Additive Manufacturing Letters 7 (2023) 100169

Contents lists available at ScienceDirect

Additive Manufacturing Letters

journal homepage: www.elsevier.com/locate/addlet

Short Communication

Effect of interlayer temperature on melt-pool morphology in laser powder bed fusion

Qian Wang [a,*], Panagiotis (Pan) Michaleris [b], Yong Ren [a], Corey Dickman [c], Edward Reutzel [c]

[a] Department of Mechanical Engineering, The Pennsylvania State University, University Park, PA 16802, United States of America
[b] PanOptimization LLC, State College, PA 16801, United States of America
[c] Applied Research Laboratory, The Pennsylvania State University, University Park, PA 16802, United States of America

ARTICLE INFO

Keywords:
Interlayer temperature
Part-scale
Optical micrograph
Convective heat transfer

ABSTRACT

Considering the high correlation of melt-pool size and build quality of a part fabricated by a laser power bed fusion (L-PBF) process, it is important to understand what are the major thermal factors that affect melt-pool size during the build process. This paper conducts an experimental investigation on how interlayer temperature affects the melt-pool morphology through a case study of a square-canonical part of Inconel 718 built with the EOS M280 system. Interlayer temperature is the layer temperature after powder spreading but before scanning a new layer. This paper examines variations in melt-pool morphology across representative layers with a large difference in interlayer temperature. It also investigates how the melt-pool size variation is affected by local temperature change caused by switching the laser scanning direction from hatch-to-hatch within a single layer. It is observed that the melt-pool half-width has increased by 40% - 100% when the interlayer temperature has increased from 100 °C to 300 °C. On the other hand, the variation of melt-pool dimensions due to local temperature change is less significant under a low interlayer temperature at 100 °C. The difference in melt-pool dimensions due to laser turnaround gets amplified when the interlayer temperature reaches high at 300 °C. Moreover, a trend of melt-pool morphology transitioning from a conduction to a convective heat transfer mode is observed at the interlayer temperature of 300 °C. Results of this paper demonstrate that interlayer temperature plays a critical role in thermal effects on melt-pool morphology, indicating a need of controlling interlayer temperature to improve build quality.

1. Introduction

Laser powder bed fusion (L-PBF) is one important metal-based additive manufacturing (AM) process that enables fabrication of complex parts with a high geometric resolution [1]. Existing literature has demonstrated that there is a high correlation between melt-pool size and build quality [2–4]. Hence, it is expected that an ideal laser-material interaction in L-PBF should produce stable melt-pool morphology with minimum variability from layer-to-layer during the build process [5].

Melt-pool dynamics and the resulting melt-pool geometry/dimensions have been mainly studied within a single hatch or among multiple hatches within a single layer. Several papers in the literature have investigated how switching laser directions could change the melt-pool size and shape, and what are the strategies for adjusting process parameters to reduce melt-pool variations. Through in situ X-ray imaging, Martin et al. investigated the keyhole pore formation mechanism at laser turn points [6], where the pore depth and cross-sectional area with respect to distance from a laser turn point were measured and analyzed for various processing conditions. Then, a mitigation strategy of laser power adjustment was applied at post-turn scans to eliminate the pore formation process and improve the geometric quality of melt tracks. Wang et al. developed a model-based nonlinear feed-forward control to modulate the laser power so that the melt-pool cross-sectional areas post laser turns would remain the same as the cross-sectional area at the middle of the first melt-track, for various configurations of multi-track cases [7]. Note that preheating temperature could also affect the size and shape of melt-pools. Chen et al. analyzed the melt-pool morphology variation of single-scan tracks of Inconel 718 under different preheating temperatures [8]. Their study showed that the melt-pool depth under a laser power of 285 W with a scan speed of 1000 mm/s increased by 31% when the preheating temperature was increased from 100 °C to 500 °C.

* Corresponding author.
E-mail address: quw6@psu.edu (Q. Wang).

https://doi.org/10.1016/j.addlet.2023.100169
Received 3 July 2023; Received in revised form 31 July 2023; Accepted 12 August 2023
Available online 22 August 2023

Overall, the aforementioned studies examined the effect of local (intra-/inter-hatch) temperature increase on the resulting overheating and expansion of melt-pools. With the ever-increasing research interest in part-scale models for thermal-mechanical analysis to support the industry's needs in fabricating sizable parts with L-PBF [9–17], one imminent task is to investigate how the part-level thermal evolution would affect the melt-pool morphology from layer-to-layer during the build process. Promoppatum et al. illustrated the melt-pool morphology variation along the build direction qualitatively [18]. However, for the six melt-pools selected for demonstration in their study, only the exposed area of each melt-pool that was not covered by adjacent layers was measured, and hence the resulting measurements did not reflect the actual melt-pool dimensions as they were masked by remelting of the subsequent layers. Williams et al. investigated how interlayer cooling time affected the layer solid- and powder-surface temperatures and the resulting melt-pool surface area, porosity and microstructure, through a build scenario of cylinders with different heights in 316L stainless steel [19].

This paper is motivated to quantify how part-level temperature evolution would affect the change of melt-pool morphology, and how such effect is compared to the effect of intra-/inter-hatch temperature variation on melt-pool morphology within a single layer. This study leverages the in-situ measurements of interlayer temperature from the authors' prior work [20], where a full evolution history of interlayer temperature during the entire build process of a square-canonical geometry of Inconel 718 on the EOS M280 was captured and analyzed. Interlayer temperature refers to the temperature distribution of the layer that has just been completed and the powder has been spread. It is taken immediately preceding the start of laser exposure on the new powder layer [17,21]. As a result, interlayer temperature serves as the initial temperature distribution under which a new layer is built. For a given point of interest, the interlayer temperature value at that point can be extracted from the distribution.

The experimental results in [20] showed that the evolution of interlayer temperature highly correlates with geometric features of the part and the support structures used to build the part. For the same geometry in [20], novel experiments are designed in this study so that the melt-pool morphologies at two selected part-layers that have a large difference in interlayer temperature are captured and compared. The effect of interlayer temperature as well as the effect of intra-/inter-hatch temperature variation on melt-pool morphology is analyzed to understand which thermal condition under investigation plays a dominant role in affecting melt-pool morphology. One main contribution of this paper lies in experimentally quantifying the effect of interlayer temperature on melt-pool morphology explicitly. Compared to the study by Williams et al. [19] that only measured melt-pool surface areas through in situ thermal imaging, this study focuses on melt-pool cross-sections that allow the measurement of melt-pool depth in addition to width, noting that melt-pool depth is a critical measure for keyholes. Furthermore, it is worth pointing out that the interlayer temperature values used in the study are coming from the build process of a complex geometry under normal, rather than artificially designed, processing conditions. Hence, the results from this study have a practical sense and are expected to shed light on identifying critical thermal variables that need to be controlled to achieve a stable and uniform melt-pool morphology during the build process of a sizable part to improve build quality.

2. Method and materials

2.1. Part geometry, build configurations, and part-scale thermal profile

This study considers the same twin square-canonical geometry of Inconel 718 as in [20] (see Fig. 1(a)). This geometry is selected because there exists a significant variation of interlayer temperature (80 °C - 300 °C) during the build process. Such large variations in interlayer temperature are direct results of the part's geometric features under normal processing conditions and normal use of support structures. Eliminating support structures in the build process could further raise up the peak interlayer temperature but would harm the buildability of the part, and it also does not reflect the real practice that commonly uses support structures.

The twin parts are built on a tool steel substrate of 252 mm × 252 mm × 30 mm by the EOS M280 L-PBF system. Each part has 1270 layers with external dimensions of 64.24 mm × 64.24 mm × 50.8 mm. It consists of an outer wall and an inner wall. The two walls are separated at lower layers, then merged into a juncture at Layer 1020 and again separated at Layer 1144 till the end. The thickness of the outer wall is 2.29 mm and the thickness of the inner wall is 0.83 mm at its early layers. Porous support structures of Inconel 718 are used during the build process. The support xy cross-section is composed of thin-walled square honeycomb (see Fig. 2 in Sec. 2) with wall spacing of 0.82 mm and wall thickness of 0.12 mm. The inner wall surface of the canonical part starts to touch the support at Layer 894, as shown in the mid-section view of the part in Fig. 1(b-c). The bottom center of the substrate is heated to 80 °C during the build process, as confirmed by the thermocouple (TC) measurements on the build plate. Fig. 1(d) shows the TC locations on the top surface of the build plate. A laser power of 285 W with a scan speed of 960 mm/s is used to scan the part, and the supports are built with a laser power of 100 W and a scan speed of 900 mm/s. Each layer has a thickness of 40 μm. A hatched stripe pattern is applied for laser scanning with a stripe width of 10 mm, a hatch spacing of 110 μm and an initial angle of 11.5°, followed by a rotation angle of 67° from layer to layer.

In-situ measurements of interlayer temperature were performed by Wang et al. using an infrared-camera based thermographic imaging [20]. The interlayer temperature distributions at several selected layers (Layer 300, 894, 1020 and 1265) are given in the Appendix. It can be seen that at each layer, the interlayer temperature values within each part component (either inner-wall or outer-wall component) are quite uniform, whereas there could be large difference in temperature between the different components in the same layer. In addition to the temperature distributions on the xy plane, individual interlayer temperature values at several selected interrogation locations during the build process are extracted. Specifically, four sample locations are picked from each square-canonical part, where P1 - P4 are selected from the left canonical part and P5 - P8 are from the right canonical part (Fig. 1(d)). For each part, two locations are chosen from the outer wall (P1/P5 and P4/P8) and two locations are chosen from the inner wall (P2/P6 and P3/P7). Fig. 1(b) shows the path of each interrogation location during the build process on the part STL.

Fig. 1(e) shows the interlayer-temperature evolution at P5 - P8 on the right canonical part. The temperature histories at P1 - P4 on the left canonical part have a similar trend to their counterparts P5 - P8 and thus are omitted here. The rapid increase in temperature at P6 and P7 on the inner wall was due to its mass growth without a sufficient path for the accumulated heat to conduct into the substrate. However, as the distance between the support and part decreases considerably, the heat conduction through powder becomes more significant [22]. As a result, the inner-wall temperature reaches its peak value before the part touches the support at Layer 894. At Layer 894, the support provides an additional path of heat transfer to the substrate and thus has caused a drastic drop in the inner-wall temperature.

With the objective of investigating the correlation between interlayer temperature and melt-pool size, each final part was then sliced at its mid-section along y-direction (Fig. 1(c) and (f)) for optical micrograph. Figs. 1(g-h) show the melt-pool cross-section images at two selected areas that have approximately the largest difference in interlayer temperature (200 °C difference), where Area 1 is around Layer 300 for which the interlayer temperature is about 100 °C and Area 2 is right below Layer 894 for which the interlayer temperature is close to the peak value of 300 °C. Note that the melt-pools are not aligned from layer to layer along the build direction due to the initial scanning angle

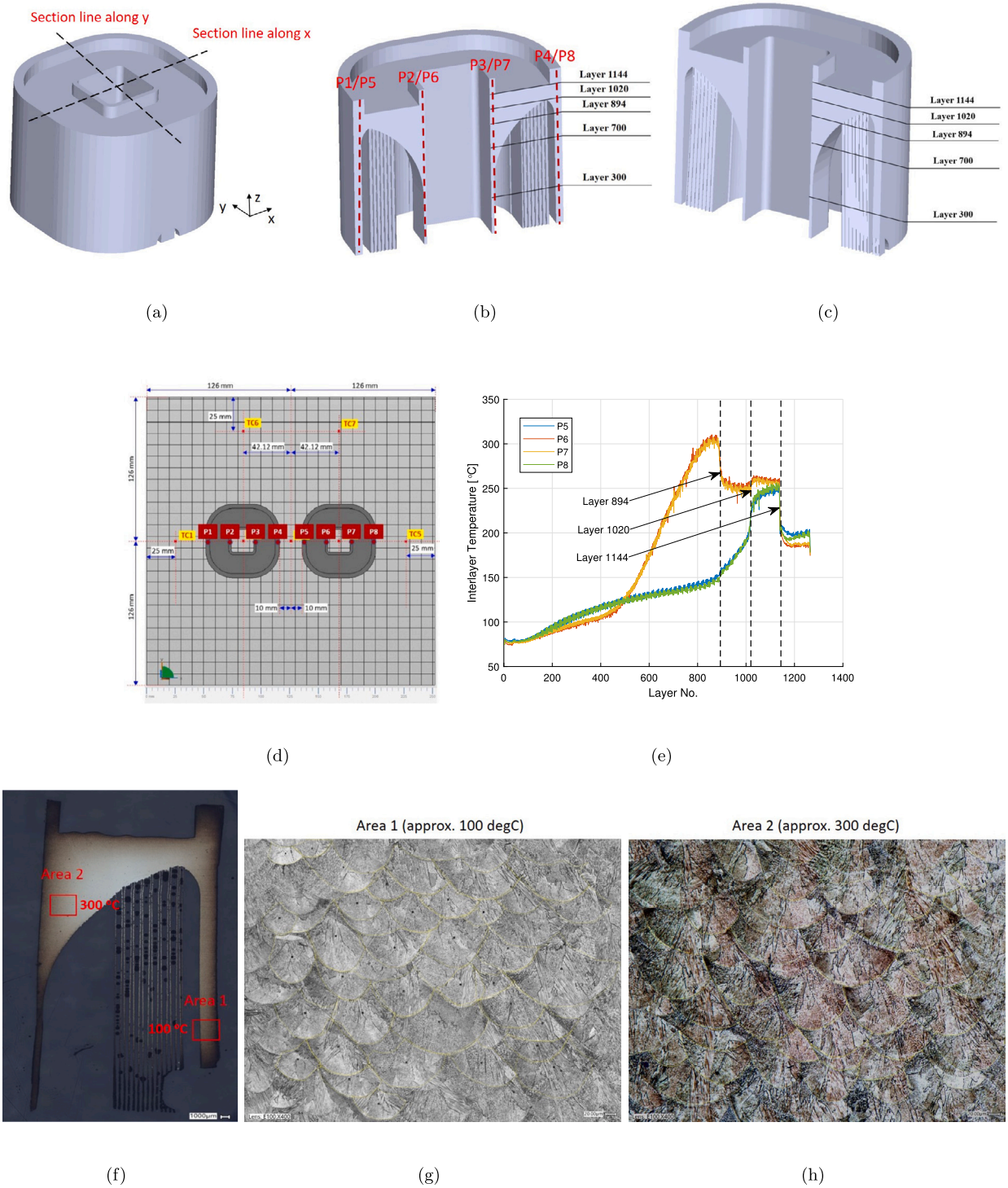

Fig. 1. Square-canonical geometry [20]. (a) STL. (b) x-midsection view. (c) y-midsection view. (d) Top view of twin parts on the build plate, where P1 - P8 denote selected locations, and TC denotes thermocouple on the build plate. (e) Interlayer temperature at P5 - P8. (f) Mid-slice along y-direction. (g-h) Optical micrograph of mid-slice at Area 1 (100 °C) and Area 2 (300 °C).

and subsequent rotation angles. Moreover, there are overlaps between melt-pools at adjacent layers due to remelting from layer to layer. Consequently, it is impossible to identify actual melt-pool dimensions from the optical micrographs shown in Figs. 1(g-h). This demonstrates that it is impossible to use the results from our prior research [20] to elucidate key difference in micrographs of areas with a large difference in interlayer temperature, which motivates developing new experimental designs in this study.

2.2. Experimental procedure of this study

Fig. 2 illustrates the experimental procedure conducted in this study to understand the effect of interlayer temperature on melt-pool morphology. The baseline canonical build (*Step 0*) refers to the build plan described in Sec. 2.1. In this study, the process parameters are kept the same. However, in contrast to applying an initial scanning angle of 11.5° followed by a rotation angle of 67° for each subsequent layer

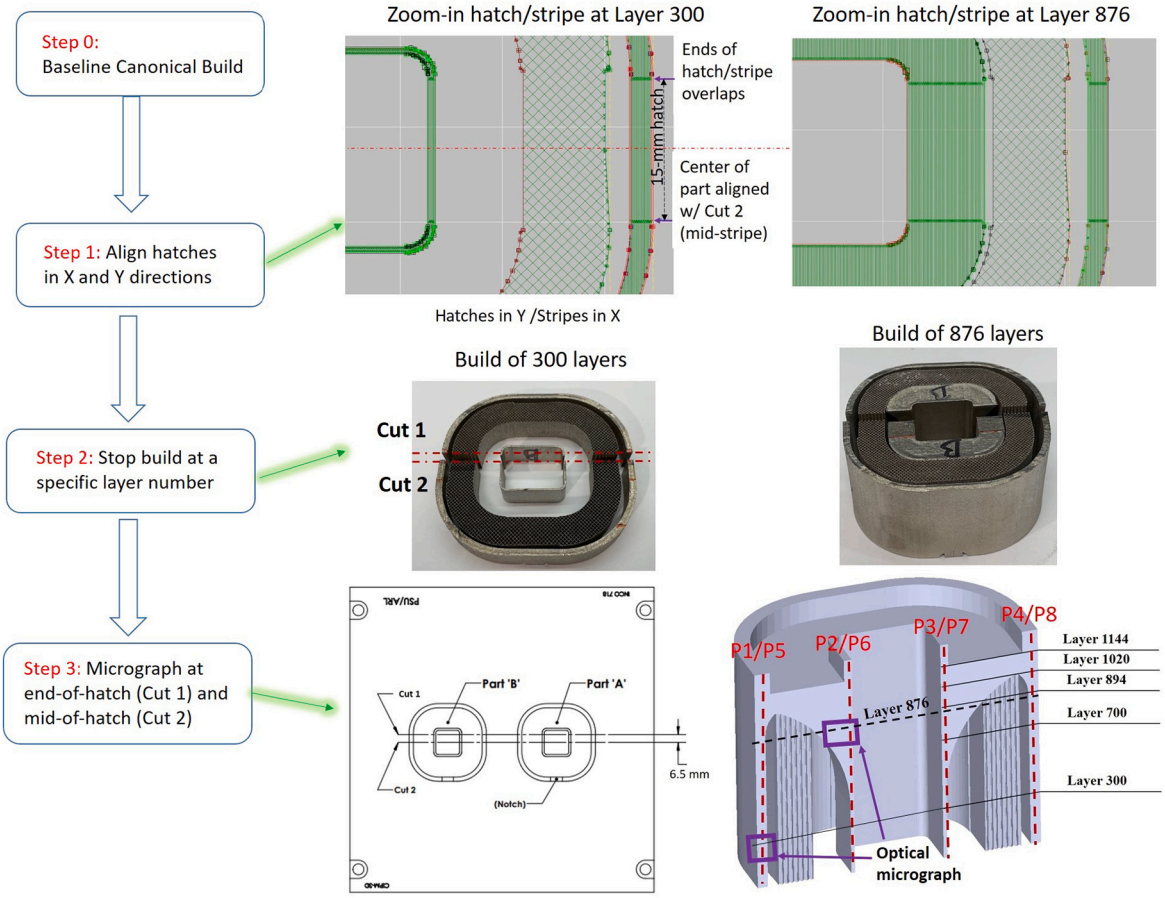

Fig. 2. Flowchart to illustrate the experimental procedure.

as in Sec. 2.1, the build plan is redesigned to align hatches in X and Y directions, with a 90° rotation angle from layer to layer (*Step 1*).

Step 1 allows alignment of melt-pools from every other layer along the build direction. However, remelting in consecutive layers would still prevent measurements of actual melt-pool dimensions. To resolve this issue, two sets of parts are built: one set stops at Layer 300 and the other set stops at Layer 876 (*Step 2)*. Zoom-in plots of hatches/stripes at Layer 300 and at Layer 876 are given in Fig. 2. The rationale behind choosing these two representative layers is given as follows. First, there is a significant difference in interlayer temperature between certain areas of the two selected layers. For example, at Layer 300, the average interlayer temperatures at both the inner- and outer-wall are approximately 100 °C, while at Layer 876, the average interlayer temperature at the inner wall is about 300 °C. Hence, there is about 200 °C difference between Layer 300 and the inner wall of Layer 876. Second, as the support starts to touch the inner wall at Layer 894 to cause a sudden temperature drop, a part layer that is slightly lower than Layer 894 should be chosen to ensure that the support is absolutely not in contact with the inner wall. Lastly, due to the 90° rotation angle for scanning from layer to layer, an even layer has to be chosen so that its hatch/stripe is aligned with the hatch/stripe in Layer 300. This new scanning pattern enables that when a cross-section is made, the melt-pool cross-sections at two different layers are comparable.

Step 3 of Fig. 2 illustrates where the builds are sectioned for optical micrographs. Considering the hatch length of 15 mm, Cut 1 corresponds to the cross-section close to the end-of-hatch (6.5 mm from the center of the hatch and 1 mm from the finish of the hatch). Melt-pools at the end-of-hatch should reflect the effect of local temperature change caused by laser turnaround where laser scanning direction switches from hatch to hatch. Cut 2 corresponds to the cross-section at the mid-of-hatch, where the melt-pools reach steady state in dimensions and shape. Optical micrographs are then taken for the outer wall at Layer 300 (100 °C) and the inner wall at Layer 876 (300 °C). For Layer 300, although the average temperature of the inner wall is close to the average temperature of the outer wall, the outer wall is chosen for micrograph as it has a larger thickness (2.29 mm) than the inner wall (0.83 mm thickness) to ensure that more melt-pool cross-sections are included and the results are less affected by the wall edges.

Note that the interlayer temperature is measured after the powder has been spread where the transient thermal behavior caused by different hatch scanning strategies has been diffused [20,22]. Consequently, the measured interlayer temperature does not abruptly shift or change due to scan directions; but instead, it is primarily influenced by part geometry. Hence, it is rational to consider that the different scan rotation used in this study, with the same laser parameters, would result in very similar interlayer temperatures (with negligible difference) as in the previous study [20].

3. Results and discussion

Fig. 3 shows the optical micrograph images of melt-pool cross-sections for the outer wall at Layer 300 and for the inner wall at Layer 876. At mid-of-hatch (Fig. 3(a) and (c)), the melt-pool cross-sections appear to have quite uniform sizes as expected. At end-of-hatch (Fig. 3(b) and (d)), melt-pools have alternating sizes as the heat buildup after each laser turnaround will result in a larger melt-pool size than the pre-turn scan. Table 1 summarizes the melt-pool dimensions measured from the melt-pool cross-sections, and Fig. 4 illustrates how the melt-pool half-width and depth are defined. The melt-pool aspect ratio, defined as the ratio of depth over half-width, is computed from the corresponding measured melt-pool dimensions. For melt-pool cross-sections at the end-of-hatch, only the (larger) melt-pools post laser-turns are included

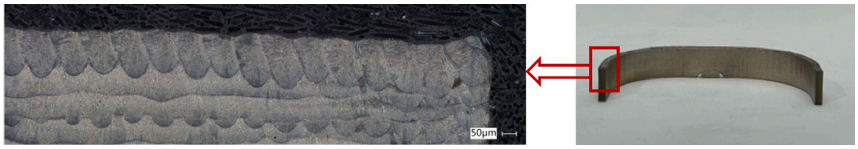

(a) Mid-of-hatch, outer-wall, Layer 300,

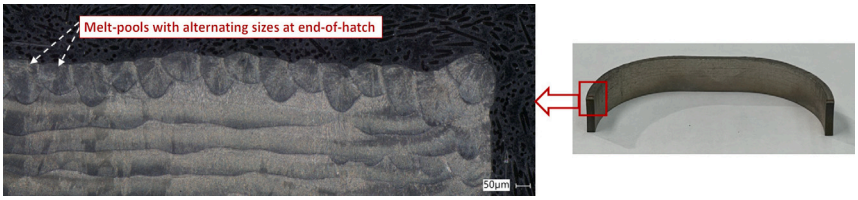

(b) End-of-hatch, outer-wall, Layer 300

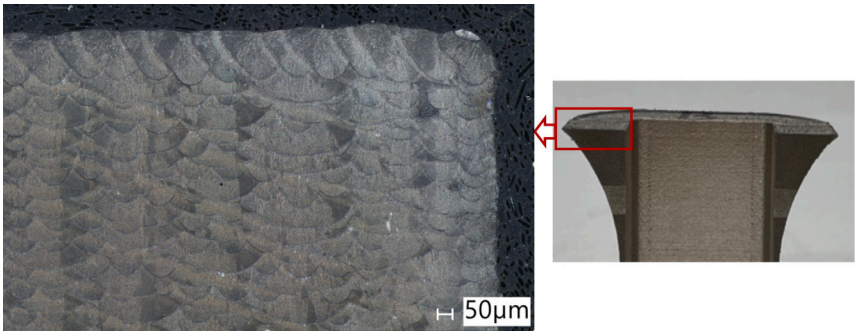

(c) Mid-of-hatch, inner-wall, Layer 876

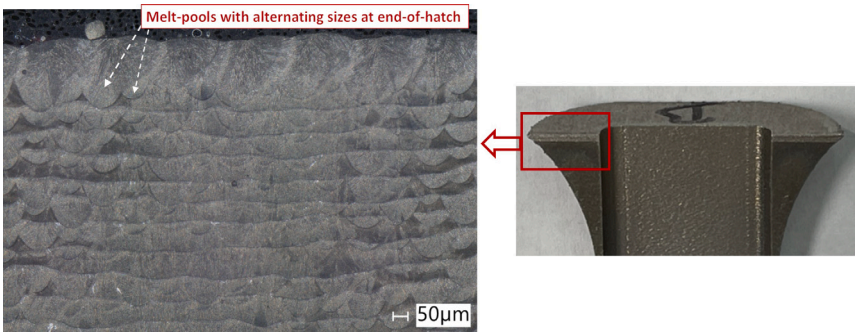

(d) End-of-hatch, inner-wall, Layer 876

Fig. 3. Optical micrograph of cross-sections: (a-b) Outer-wall at Layer 300; (c-d) Inner-wall at Layer 876.

in the dimension statistics given in Table 1 to evaluate how the local temperature change, caused by switching laser scanning directions, affects the melt-pool size.

Table 2 gives the percentage of change in mean melt-pool dimensions (half-width and depth) caused by laser turnaround and/or interlayer temperature, where the melt-pool dimensions for the mid-of-hatch at Layer 300 are used as the baseline. To compare the mean values of two groups with different number of melt-pool samples, p-value is calculated using the unequal variance t-test. For $p > 0.05$, it is deemed that the difference in group means is not statistically significant.

Table 2 shows that when the interlayer temperature has increased from 100 °C at Layer 300 to 300 °C at Layer 876, the melt-pool mean half-width at the mid-of-hatch has increased by about 40%. When the interlayer temperature is relatively low at Layer 300, the effect of local intra-/inter-hatch temperature change on melt-pool half-width is small and the effect on the melt-pool depth is statistically not differentiable. When the interlayer temperature reaches high to 300 °C at Layer 876, the difference in melt-pool dimensions due to laser turnaround gets considerably amplified, e.g., the end-of-hatch has about 100% increase in the melt-pool mean half-width compared to the baseline (or about 40% increase compared to the mid-of-hatch in the same layer); and similarly, the end-of-hatch has about 27% increase in melt-pool mean depth compared to the baseline.

Fig. 3 demonstrates that interlayer temperature has also changed the melt-pool shape visibly. Note that all melt-pool aspect ratios given in Table 1 are greater than one but less than two. However, the melt pools at Layer 300 have smooth boundaries in a half-ellipsoidal shape. In contrast, the melt-pool cross-sections at Layer 876 appear to be composed

Table 1
Mean and standard deviation of melt-pool dimensions (μm) and aspect ratio (ratio of depth over half-width). Only the post-turn larger melt-pools are included for the end-of-hatch statistics.

Layer no.	Mid-of-hatch (steady-state)			End-of-hatch (post-turn)		
	half-width (μm)	depth (μm)	aspect ratio	half-width (μm)	depth (μm)	aspect ratio
300 (100 °C)	89.6 ± 5.5	173.9 ± 13.4	1.94 ± 0.15	76.4 ± 7.2	161.8 ± 14.8	2.15 ± 0.37
876 (300 °C)	125.7 ± 11.7	167.1 ± 12.0	1.34 ± 0.15	179.3 ± 14.6	220.2 ± 27.4	1.24 ± 0.19

Table 2
Percentage of change in melt-pool mean half-width and in mean depth caused by laser turnaround and/or interlayer temperature, where the melt-pool dimensions at mid-of-hatch of Layer 300 are used as the baseline to compute the percentage of change. P-value is calculated using unequal variance t-test; for $p > 0.05$, % of change is deemed not statistically significant.

Cases	Mean half-width		Mean depth	
	value (μm)	% of change (p-value)	value (μm)	% of change (p-value)
Base: (Layer 300, 100 °C, mid-of-hatch)	89.6	0%	173.9	0%
(Layer 300, 100 °C, end-of-hatch)	76.4	-14.8% ($p = 0.001$)	161.8	-6.9% ($p = 0.1$)
(Layer 876, 300 °C, mid-of-hatch)	125.7	40.3% ($p < 0.001$)	167.1	-3.9% ($p = 0.2$)
(Layer 876, 300 °C, end-of-hatch)	179.3	100.1% ($p < 0.001$)	220.2	26.7% ($p < 0.001$)

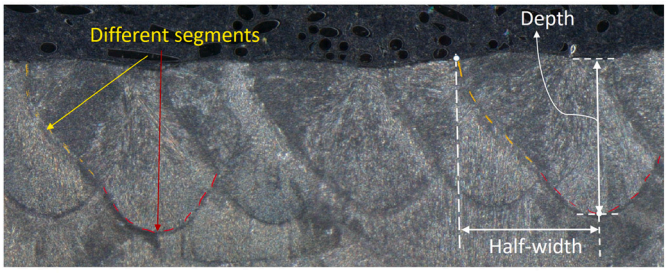

Fig. 4. Measures of melt-pool geometry (zoom-in melt-pool cross-sections at mid-of-hatch, inner-wall, Layer 876). The melt-pool geometry at inner-wall of Layer 876 demonstrates transition towards a convection dominated heat transfer mode, where the top-region (boundary outlined by yellow dashed line) resembles a wide hourglass but the bottom of the melt-pool (boundary outlined by red dashed line) resembles a narrower teardrop bottom.

of two regions (see Fig. 4), where the top region (boundary outlined by a yellow dashed line) resembles a wide hourglass but the bottom of the melt-pool (boundary outlined by a red dashed line) resembles a narrower teardrop bottom. Such melt-pool morphology at Layer 876 is an indicator of transition from a conduction-dominated heat transfer mode to a more convection-dominated heat transfer mode. It is interesting to see that the average depth-over-half-width ratios for Layer 876, where the average ratio is 1.34 for the mid-of-hatch and 1.24 for the end-of-hatch, are smaller than their counterparts at Layer 300, where the average ratio is 1.94 for the mid-of-hatch and 2.15 for the end-of-hatch. This suggests that as long as the aspect ratio is larger than one but not much larger than one, the limited difference in the aspect ratio itself might not be a good indicator for the relative ratio of convection versus conduction heat transfer within the melt pool. Note that such relative ratio of convection over conduction is commonly described by the Peclet number [23].

In summary, Fig. 3 and Tables 1-2 indicate that interlayer temperature plays a major role in affecting the melt-pool size and affecting the melt-pool into a more convection-dominated heat transfer mode. The intra-/inter-hatch local temperature variation has a much less significant impact when the interlayer temperature is low, and it only gets amplified when the interlayer temperature is high. Such observation strongly motivates future research to emphasize the control of interlayer temperature to achieve a more uniform melt-pool size throughout the build process. Intra-/inter-hatch process control within a layer is secondary when the interlayer temperature is under control.

4. Conclusions

This paper has conducted an experimental study to investigate how interlayer temperature affects the melt-pool morphology during the build process, through a case study of a square-canonical part of Inconel 718 built with the EOS M280 system. Identifying melt-pool dimensions at a representative layer is made possible by re-designing the hatch scanning strategy, where the hatches/stripes are first aligned in the X and Y directions followed by a 90° rotation angle from layer to layer, and then the build is stopped at the exact layer of interest. Such build plan has enabled the melt-pool cross-sections at chosen layers not skewed or covered by subsequent layers so that they become comparable. The effect of part-level temperature on the change of melt-pool dimensions and melt-pool shape is compared to the effect due to local intra/inter-hatch temperature variation caused by switching laser directions from hatch to hatch within a single layer. Measurements from the optical micrographs of melt-pool cross-sections show that the melt-pool mean half-width at the mid-of-hatch has increased by 40% when the interlayer temperature has increased from 100°C to 300 °C. In contrast, the effect of local intra-/inter-hatch temperature variation on melt-pool size change is much less significant when the interlayer temperature is low (at 100 °C). Such local temperature effect seems to only get amplified at a high interlayer temperature (300 °C), enabling a 40% increase in melt-pool mean half-width at the end-of-hatch compared to the mid-of-hatch in the same layer (or 100% increase compared to the mid-of-hatch at the layer with 100 °C interlayer temperature). Overall, results from this study indicate that part-level temperature such as interlayer temperature is one dominant thermal variable that affects melt-pool morphology during the build process, suggesting the control of interlayer temperature as a potential primary knob to improve build quality.

Declaration of competing interest

The authors declare that they have no known competing financial interests or personal relationships that could have appeared to influence the work reported in this paper.

Data availability

Data will be made available on request.

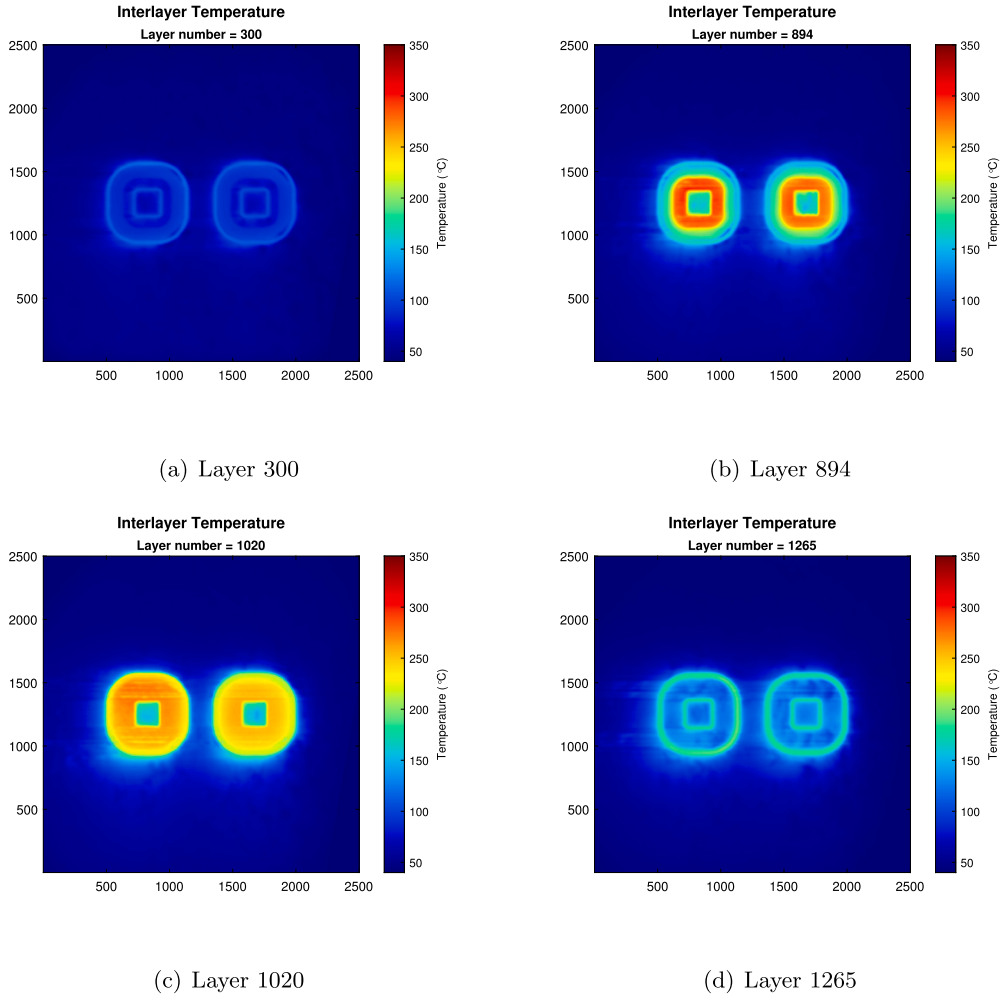

(a) Layer 300

(b) Layer 894

(c) Layer 1020

(d) Layer 1265

Fig. 5. Interlayer temperature distributions at selected layers [20].

Acknowledgement

This work was supported in part by the U.S. National Science Foundation under Grant No. 2015930. The authors would also like to thank Mr. Scott Tokarz at the Applied Research Lab of Penn State for his work on optical micrograph of the experimental samples.

Appendix A. Interlayer temperature distributions at selected layers

Fig. 5 shows the interlayer temperature distributions at several representative layers.

References

[1] S. Cooke, K. Ahmadi, S. Willerth, R. Herring, Metal additive manufacturing: technology, metallurgy and modelling, J. Manuf. Process. 57 (2020) 978–1003.

[2] J. Dilip, S. Zhang, C. Teng, K. Zeng, C. Robinson, D. Pal, B. Stucker, Influence of processing parameters on the evolution of melt pool, porosity, and microstructures in Ti-6Al-4V alloy parts fabricated by selective laser melting, Prog. Addit. Manuf. 2 (3) (2017) 157–167.

[3] P. Kumar, J. Farah, J. Akram, C. Teng, J. Ginn, M. Misra, Influence of laser processing parameters on porosity in Inconel 718 during additive manufacturing, Int. J. Adv. Manuf. Technol. 103 (1–4) (2019) 1497–1507.

[4] J. Ning, D.E. Sievers, H. Garmestani, S.Y. Liang, Analytical modeling of part porosity in metal additive manufacturing, Int. J. Mech. Sci. 172 (2020) 105428.

[5] S. Patel, M. Vlasea, Melting modes in laser powder bed fusion, Materialia 9 (2020) 100591.

[6] A.A. Martin, N.P. Calta, S.A. Khairallah, J. Wang, P.J. Depond, A.Y. Fong, V. Thampy, G.M. Guss, A.M. Kiss, K.H. Stone, et al., Dynamics of pore formation during laser powder bed fusion additive manufacturing, Nat. Commun. 10 (1) (2019) 1987.

[7] Q. Wang, P.P. Michaleris, A.R. Nassar, J.E. Irwin, Y. Ren, C.B. Stutzman, Model-based feedforward control of laser powder bed fusion additive manufacturing, Addit. Manuf. 31 (2020) 100985.

[8] Q. Chen, Y. Zhao, S. Strayer, Y. Zhao, K. Aoyagi, Y. Koizumi, A. Chiba, W. Xiong, A.C. To, Elucidating the effect of preheating temperature on melt pool morphology variation in Inconel 718 laser powder bed fusion via simulation and experiment, Addit. Manuf. 37 (2021) 101642.

[9] F. Dugast, P. Apostolou, A. Fernandez, W. Dong, Q. Chen, S. Strayer, R. Wicker, A.C. To, Part-scale thermal process modeling for laser powder bed fusion with matrix-free method and GPU computing, Addit. Manuf. 37 (2021) 101732.

[10] S. Kolossov, E. Boillat, R. Glardon, P. Fischer, M. Locher, 3D FE simulation for temperature evolution in the selective laser sintering process, Int. J. Mach. Tools Manuf. 44 (2–3) (2004) 117–123.

[11] J. Yin, H. Zhu, L. Ke, W. Lei, C. Dai, D. Zuo, Simulation of temperature distribution in single metallic powder layer for laser micro-sintering, Comput. Mater. Sci. 53 (1) (2012) 333–339.

[12] I. Roberts, C. Wang, R. Esterlein, M. Stanford, D. Mynors, A three-dimensional finite element analysis of the temperature field during laser melting of metal powders in additive layer manufacturing, Int. J. Mach. Tools Manuf. 49 (12) (2009) 916–923.

[13] N. Contuzzi, S. Campanelli, A. Ludovico, 3D finite element analysis in the selective laser melting process, Int. J. Simul. Model. 10 (3) (2011) 113–121.

[14] C. Li, C. Fu, Y. Guo, F. Fang, A multiscale modeling approach for fast prediction of part distortion in selective laser melting, J. Mater. Process. Technol. 229 (2016) 703–712.

[15] N. Hodge, R. Ferencz, J. Solberg, Implementation of a thermomechanical model for the simulation of selective laser melting, Comput. Mech. 54 (1) (2014) 33–51.

[16] J. Schilp, C. Seidel, H. Krauss, J. Weirather, Investigations on temperature fields during laser beam melting by means of process monitoring and multiscale process modelling, Adv. Mech. Eng. 6 (2014) 217584.

[17] M. Gouge, E. Denlinger, J. Irwin, C. Li, P. Michaleris, Experimental validation of thermo-mechanical part-scale modeling for laser powder bed fusion processes, Addit. Manuf. (2019).
[18] P. Promoppatum, S.-C. Yao, P.C. Pistorius, A.D. Rollett, P.J. Coutts, F. Lia, R. Martukanitz, Numerical modeling and experimental validation of thermal history and microstructure for additive manufacturing of an Inconel 718 product, Prog. Addit. Manuf. 3 (1) (2018) 15–32.
[19] R.J. Williams, A. Piglione, T. Rønneberg, C. Jones, M.-S. Pham, C.M. Davies, P.A. Hooper, In situ thermography for laser powder bed fusion: effects of layer temperature on porosity, microstructure and mechanical properties, Addit. Manuf. 30 (2019) 100880.
[20] Q. Wang, P. Michaleris, M. Pantano, C. Li, Y. Ren, A.R. Nassar, Part-scale thermal evolution and post-process distortion of Inconel-718 builds fabricated by laser powder bed fusion, J. Manuf. Process. 81 (2022) 865–880.
[21] C. Li, M.F. Gouge, E.R. Denlinger, J.E. Irwin, P. Michaleris, Estimation of part-to-powder heat losses as surface convection in laser powder bed fusion, Addit. Manuf. 26 (2019) 258–269.
[22] Y. Ren, Q. Wang, A finite difference method for fast prediction and control of part-scale temperature evolution in laser powder bed fusion, J. Manuf. Process. 93 (2023) 299–314.
[23] R. Rai, G. Roy, T. DebRoy, A computationally efficient model of convective heat transfer and solidification characteristics during keyhole mode laser welding, J. Appl. Phys. 101 (5) (2007) 054909.